ACS OMEGA

http://pubs.acs.org/journal/acsodf

Article

Fabrication of α-Fe_2O_3 Nanostructures: Synthesis, Characterization, and Their Promising Application in the Treatment of Carcinoma A549 Lung Cancer Cells

Indresh Kumar, Rashmi Nayak, Lal Babu Chaudhary, Vashist Narayan Pandey, Sheo K. Mishra, Narendra Kumar Singh, Abhishek Srivastava, Surendra Prasad, and Radhey Mohan Naik*

Cite This: *ACS Omega* 2022, 7, 21882−21890

Read Online

ACCESS | Metrics & More | Article Recommendations

ABSTRACT: In the present work, iron nanoparticles were synthesized in the α-Fe_2O_3 phase with the reduction of potassium hexachloroferrate(III) by using L-ascorbic acid as a reducing agent in the presence of an amphiphilic non-ionic polyethylene glycol surfactant in an aqueous solution. The synthesized α-Fe_2O_3 NPs were characterized by powder X-ray diffraction, field emission scanning electron microscopy, transmission electron microscopy, atomic force microscopy, dynamic light scattering, energy dispersive X-ray spectroscopy, Fourier transform infrared spectroscopy, and ultraviolet−visible spectrophotometry. The powder X-ray diffraction analysis result confirmed the formation of α-Fe_2O_3 NPs, and the average crystallite size was found to be 45 nm. The other morphological studies suggested that α-Fe_2O_3 NPs were predominantly spherical in shape with a diameter ranges from 40 to 60 nm. The dynamic light scattering analysis revealed the zeta potential of α-Fe_2O_3 NPs as -28 ± 18 mV at maximum stability. The ultraviolet−visible spectrophotometry analysis shows an absorption peak at 394 nm, which is attributed to their surface plasmon vibration. The cytotoxicity test of synthesized α-Fe_2O_3 NPs was investigated against human carcinoma A549 lung cancer cells, and the biological adaptability exhibited by α-Fe_2O_3 NPs has opened a pathway to biomedical applications in the drug delivery system. Our investigation confirmed that L-ascorbic acid-coated α-Fe_2O_3 NPs with calculated $IC_{50} \leq 30$ μg/mL are the best suited as an anticancer agent, showing the promising application in the treatment of carcinoma A549 lung cancer cells.

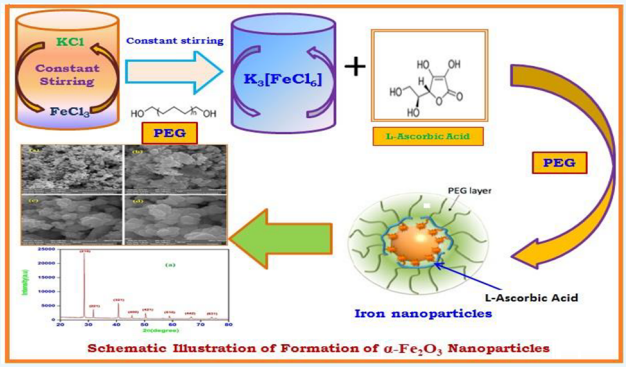

1. INTRODUCTION

In the recent past, lung cancer has been the second-most commonly diagnosed cancer in human beings worldwide. In 2019 in the United States, one-fourth of all deaths were due to lung cancer. Recent statistics show that about 228,150 new cases and 142,670 deaths could occur due to lung and bronchus cancer in the USA.[1] To improve the efficacy of lung cancer therapy and minimize its hazardous impacts on healthy tissues and organs, new treatment methods are urgently needed.[2] Recently, interdisciplinary research in nanotechnology has been an emerging area to diagnose a large number of diseases incurable to humans and disastrous to the environment.[3] Nanoparticles (NPs), therefore, in interdisciplinary nanosized fabricated nanostructures have shown potential applications in the fields of medicine, biosensors, and carcinoma treatment due to their microporous and mesoporous discipline.[4] Mesoporous materials have been synthesized using two key approaches: one is the soft-templating method and the other is the hard-templating method with desired morphology.[5] It is mostly synthesized by using the soft-templating method because of the easy approach with a low molecular weight polymer like polyethylene glycol (PEG) as a surfactant.[6,7] Many researchers have employed iron oxide nanoparticles thoroughly because of their unique properties such as low Curie temperature, high magnetic susceptibility, high surface area-to-volume ratio, high surface energy, tunable pore size, and uniform distribution, which provide a high demand for *in vivo* and *in vitro* application in the field of biomedical science to targeted drug delivery,[8] magnetic resonance imaging (MRI),[9] cancer hyperthermia,[10] catalysis,[11] biosensing,[12] environmental remediations,[13] and other industrial applications.[14] The use of iron nanoparticles in the

Received: April 4, 2022
Accepted: June 3, 2022
Published: June 13, 2022

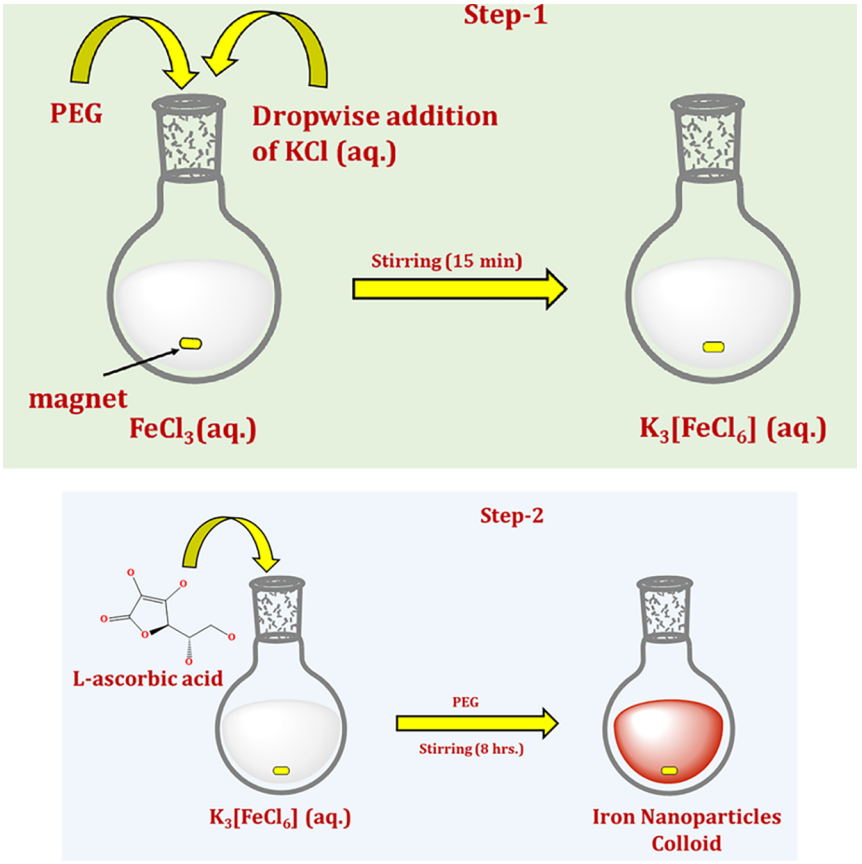

Figure 1. Systematic illustration of the synthesis of α-Fe_2O_3 NPs.

biomedical field has led to significant advantages in terms of diagnosis,[15−20] biomedical detection,[21,22] therapy,[17] and drug delivery.[14,23] The surface morphology and particle size of iron/iron oxide NPs could easily be controlled by a suitable synthetic method, which provides a specific application.[15] There are a few reports in the literature on the synthesis of iron oxide NPs, with limited applications because of large agglomeration and difficulty with dispersion in an aqueous medium, which prohibits *in vitro* application.[16,21] On the other hand, polymer-coated iron oxide NPs have gained much attention due to the balancing of magnetic and Van der Waals forces.[22] Generally, several synthesis methods such as physical, chemical, and biological methods have been employed for the preparation of iron oxide NPs. These have been investigated to produce more stable, soluble, biocompatible, and size-controlled NPs with desired shapes such as spherical,[24] nanoflowers, nanotubes, and nanowires. Several chemical routes such as sol−gel,[25−27] co-precipitations,[28] hydrothermal,[29] sonochemical,[30] microwave-assisted,[31] physical routes as spray pyrolysis,[32] chemical reduction,[23,33−35] thermal decompositions,[36] and green synthesis[37] as a biological route were used for the synthesis of metal NPs. Many researchers have successfully synthesized iron-based NPs for their application in *in vitro* and *in vivo* analysis[37−40] and obtained good results, *i.e.*, Thenmozhi *et al.* have biosynthesized and characterized iron NPs via *Syzygium aromaticum* extract and determined their cytotoxicity against breast cancer cell lines.[37] Fahmi and Chang have used a facile strategy to enable NPs for simultaneous phase transfer, folate receptor targeting, and cisplatin delivery.[41] Ebrahimi *et al.* have established a novel drug delivery system involving doxorubicin-encapsulated magnetic NPs for chemotherapeutic use to treat lung cancer cell lines.[42] An *et al.* have observed the peroxidase-like activity of Fe_3O_4@carbon NPs and found it to enhance L-ascorbic acid (LAA)-induced oxidative stress with selective damage to PC-3 prostate cancer cells.[43] Calero *et al.* have assessed the interaction of magnetic NPs with breast cancer cells.[38] Therefore, in the present study, we have planned to synthesize iron nanoparticles (α-Fe_2O_3 NPs) by using PEG as a stabilizer and L-ascorbic acid (LAA) as a reducing agent. LAA has high water solubility and excellent antioxidant property. It is an essential micronutrient due to which it has been used in cancer treatment in recent years as it exists as ascorbate at physiological pH.[44,45] However, amphiphilic non-ionic polyethylene glycol (PEG) is used for the preparation of α-Fe_2O_3 NPs because it behaves as a good stabilizing or capping agent. Moreover, PEG makes a hydrophilic protective layer around the α-Fe_2O_3 NPs surface, which enhances the half-life in the blood circulation for some time via spatial repulsion rejection. Also, PEG behaves as a bridge that is associated with the targeted ligand through its hydroxy terminal, which can easily bind with the receptors on the cell surface to enhance the targeted drug delivery capacity of α-Fe_2O_3 NPs.[46] The addition of PEG as a stabilizer can improve the efficiency of drug delivery, retard the removal of α-Fe_2O_3 NPs by the mononuclear phagocytic system (MPS), and also modify some of the physicochemical properties of α-Fe_2O_3 NPs like stability, drug loading and releasing properties, and mechanical properties of the membrane. However, several reports have already been discussed about the synthesis, characterization, and cytotoxicity test for iron NPs with an α-Fe_2O_3 phase against human carcinoma A549 lung cancer cells.[39,40] Despite

https://doi.org/10.1021/acsomega.2c02083
ACS Omega 2022, 7, 21882−21890

the fact that the issue of ejection of NP material from the human body is still not satisfactorily resolved, the performed study confirmed that the proposed α-Fe_2O_3 NPs could be a promising candidate for a potential therapeutic compound for the advanced treatment of carcinomas. Hence, this report first describes the synthesis and characterization of α-Fe_2O_3 NPs and then the α-Fe_2O_3 NPs are subjected to evaluation of the cytotoxicity toward human lung cancer cells (A549 cell lines).

2. EXPERIMENTAL SECTION

2.1. Chemicals. Anhydrous iron(III) chloride (98%, Merck), potassium chloride (98%, Merck), and analytical grade polyethylene glycol, ethanol, and L-ascorbic acid (99%) were purchased from Sigma-Aldrich. All the chemicals were utilized without further purification. Double-distilled water (DDW) was used wherever necessary. The glassware was properly washed, sanitized, and autoclaved before use. Additionally, chemicals required for the evaluation of the cytotoxicity of synthesized α-Fe_2O_3 NPs are dimethyl sulfoxide (DMSO), Dulbecco's modified Eagle medium (DMEM), 5% CO_2 and bovine serum albumin (BSA), phosphate-buffered saline (PBS), trypan blue (TB), trypsin-ethylenediaminetetra-acetic acid (TRY-EDTA) solution (0.25%), antibiotic–antimycotic (Ab/Am) solution, and 3-(4,5-dimethylthiazol-2-yl)-2,5-diphenyl tetrazolium bromide (MTT) dye.

2.2. Synthesis of α-Fe_2O_3 NPs. The synthesis of α-Fe_2O_3 NPs was initiated by mixing the aqueous solution of $FeCl_3$ and KCl in 1:3 ratios in the presence of polyethylene glycol (PEG) as a surfactant. The aqueous solution $FeCl_3$ was stirred vigorously for 15 min after the addition of PEG and KCl (aq) solution at 10,000 rpm for 8 h to obtain the $K_3[FeCl_6]$ coordination complex (step 1, Figure 1). To get the final product, 20 mL of 10 mM $K_3[FeCl_6]$ was mixed with 1 mg/mL PEG and 40 mL of 0.1 M LAA taken in a round-bottom flask (step 2, Figure 1). The well-explained procedure of the synthesis is represented in Scheme 1, and a systematic illustration of the synthesis of α-Fe_2O_3 NPs is shown in the Figure 1. The mixture was then stirred at 10,000 rpm for 3 h at room temperature. The appearance of a light reddish-brown solution in the flask confirmed the formation of α-Fe_2O_3 NPs. The formed reddish-brown solution was stirred for 2 h at 37 °C and further centrifuged at 10,000 rpm for 25 min, which has a strong plasmon band at 394 nm. After centrifugation, suspended α-Fe_2O_3 NPs were obtained and washed several times with DDW and ethanol to remove the excessive amount of PEG and other contaminants. The α-Fe_2O_3 NPs thus obtained were dried in an oven and collected for further characterization.

Scheme 1. Scheme for the Synthesis of α-Fe_2O_3 NPs

$$FeCl_3(aq) + KCl(aq) \xrightarrow{PEG\ (aq)} K_3[FeCl_6](aq) \quad (1)$$

$$K_3[FeCl_6](aq) + C_6H_8O_6(aq)\ (\text{L-ascorbic acid}) \xrightarrow{PEG\ (aq)} \text{Iron Nanoparticles (reddish-brown colloid)} \quad (2)$$

2.3. Characterization Techniques. The prepared α-Fe_2O_3 NPs were characterized by the powder X-ray diffraction (XRD) method using an X-ray diffractometer XPERT-3 operated at a voltage of 40 kV and a current of 40 kA. The patterns were recorded as a function of 2θ angle in the range of 20–80° with a step size of 0.01 at a scanning rate of 0.02 steps/s with the help of a monochromatized X-ray beam with a copper filter (Cu-Kα, λ = 1.54178 Å). The surface morphology and elemental analysis of α-Fe_2O_3 NPs were investigated by using field emission scanning electron microscopy (FE-SEM) using a JSM-6490 LV, JEOL, Tokyo, Japan. The samples were investigated by FE-SEM with an acceleration voltage of 5 kV and a current of 10 μA. The mesoporous size and shape of α-Fe_2O_3 NPs were observed using a JEOL-2100 transmission electron microscope. Moreover, a Nano Magnetic (hpSPMv1.5) atomic force microscope was also used to observe the surface morphology of α-Fe_2O_3 NPs. The hydrodynamic size and zeta potential of α-Fe_2O_3 NPs were evaluated with the help of a Zetasizer ZS90 Nano Series Malvern Instrument for dynamic light scattering (DLS). The α-Fe_2O_3 NPs were sonicated for 15 min for complete dispersion. A UV–visible double-beam spectrophotometer (Lab UV NexGen) equipped with an A-100 constant temperature sipper system was used for recording the UV–visible spectra of the colloidal α-Fe_2O_3 NPs in the region of 350–500 nm and also for the determination of the λ_{max} value. The wavenumber ($1/\lambda_{max}$) detection of the surfactant and L-ascorbic acid was estimated through a Fourier transform infrared (FTIR) spectrophotometer (Shimadzu: IR Affinity-1S).

3. RESULTS AND DISCUSSION

3.1. Powder XRD Study of α-Fe_2O_3 NPs. The powder XRD pattern is a useful tool for determining the structural

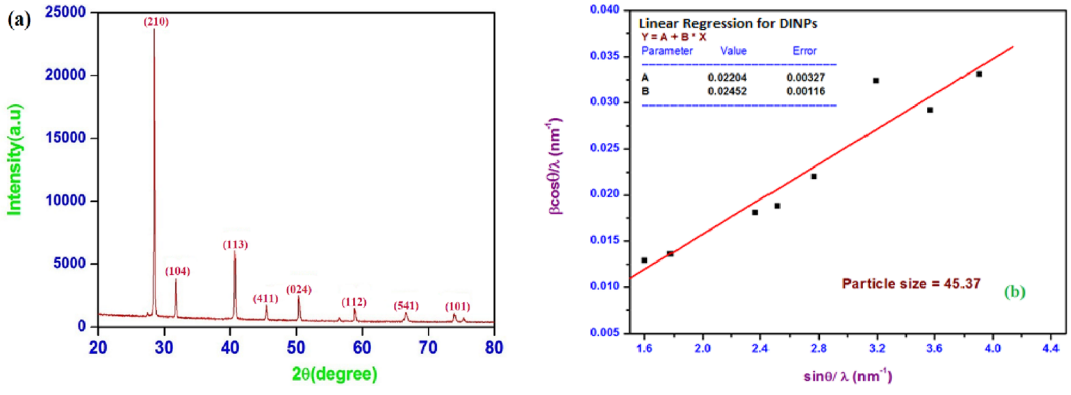

Figure 2. (a) Powder X-ray diffraction analysis and (b) Williamson-Hall plot of α-Fe_2O_3 NPs.

https://doi.org/10.1021/acsomega.2c02083
ACS Omega 2022, 7, 21882–21890

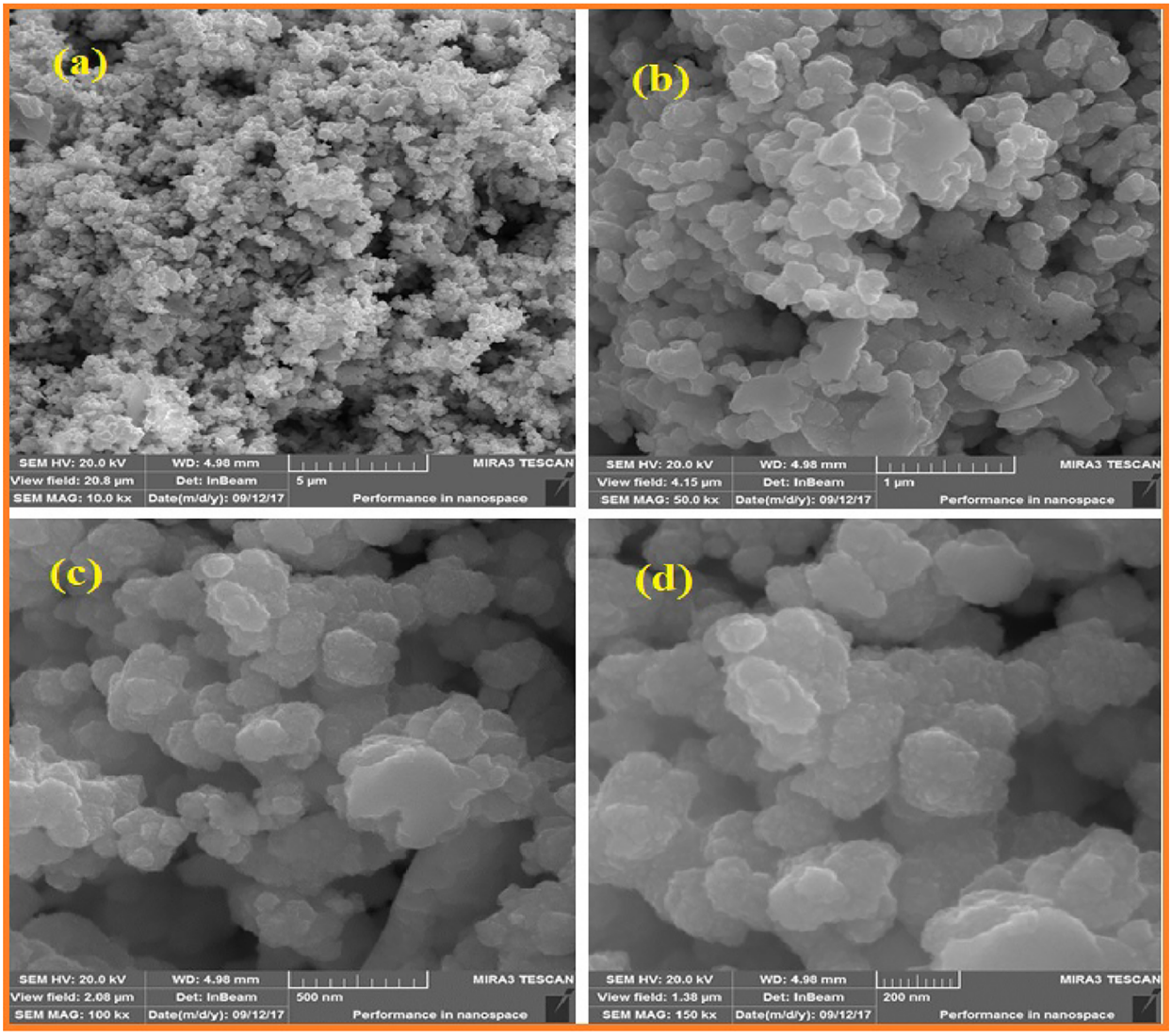

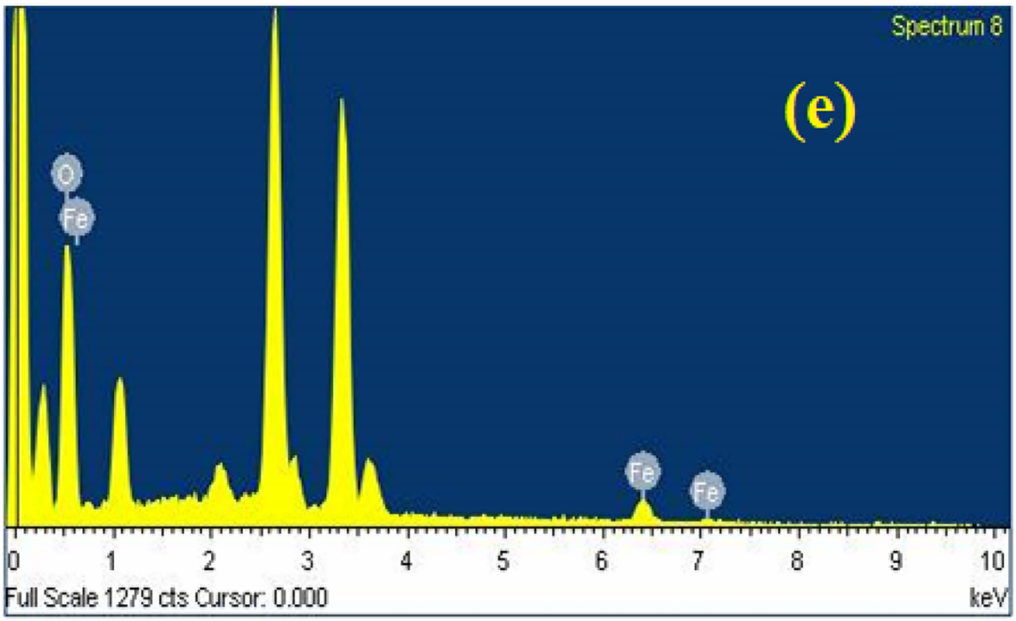

Figure 3. (a–d) FE-SEM images and (e) EDX profile of α-Fe_2O_3 NPs.

https://doi.org/10.1021/acsomega.2c02083
ACS Omega 2022, 7, 21882–21890

phase and crystallite size of the synthesized α-Fe_2O_3 NPs. The degree of crystallinity of the synthesized α-Fe_2O_3 NPs was determined via powder XRD analysis. Figure 2a shows powder XRD patterns of α-Fe_2O_3 NPs having a number of characteristic peaks (2θ) at diffraction angles of 28.43°, 32.03°, 40.62°, 45.31°, 50.23°, 58.56°, 66.61°, and 74.14° corresponding to indices (210), (104), (113), (411), (024), (112), (541), and (101), respectively. The crystal structure of α-Fe_2O_3 NPs was well matched with JCPDS card numbers 33-0664 and 34-1266.[47−49] The average crystallite size (D) of synthesized α-Fe_2O_3 NPs was calculated using Debye−Scherrer's relation and was found to be 45 nm (mesoporous range). The Williamson-Hall (W-H) plot given in Figure 2b was also used to calculate the grain size as well as the strain of the α-Fe_2O_3 NPs.[33]

$$\beta \cos \theta/\lambda = \frac{k}{D} + \varepsilon \sin \theta/\lambda \quad (1)$$

$$\delta = 1/D^2 \quad (2)$$

The W-H plot depicted the plot of $\beta \cos \theta/\lambda$ against $\varepsilon \sin \theta/\lambda$ from which strain (ε) was calculated from the slope of the straight line (eq 1). The crystallite size was estimated from the intercept on $\beta \cos \theta/\lambda$ corresponding to zero strain. The strain (ε) and crystallite size (D) of synthesized α-Fe_2O_3 NPs were calculated and found to be 0.02452 and 45.37 nm, respectively, where a positive sign indicated tensile strain. The strain in α-Fe_2O_3 NPs is due to the defects arising from cation and anion vacancies. It also explains the little agglomeration by weak Van der Waals forces. The line dislocation density (δ) of α-Fe_2O_3 NPs was 4.858×10^{14} m^{-2} calculated by using eq 2.

3.2. Analysis of the Morphology of α-Fe_2O_3 NPs. The morphological analysis of α-Fe_2O_3 NPs is shown in Figure 3a−d as FE-SEM micrographs. The FE-SEM micrographs of α-Fe_2O_3 NPs at different magnifications including 10.0 kx, 50.0 kx, 100.0 kx, and 150.0 kx are shown in Figure 3a−d. These FE-SEM micrographs show that α-Fe_2O_3 NPs are of spherical shape with the size range between 40 and 60 nm. Moreover, a little agglomeration was observed in FE-SEM micrographs. This might be due to the strong attractive interaction between the oxy (−O−) groups of PEG. It also reveals that the surface of α-Fe_2O_3 NPs is closely packed. The FE-SEM micrographs of α-Fe_2O_3 NPs show good resemblance with the result reported by Kuang *et al.* for the synthesis of α-Fe_2O_3 NPs obtained by using tea leaf extract.[50] The observed irregularity in FE-SEM images indicates that the prepared α-Fe_2O_3 NPs contain a large volume of heat. The composition of synthesized α-Fe_2O_3 NPs was investigated by using energy dispersive X-ray (EDX) spectroscopy analysis as shown in Figure 3e. The EDX profile confirmed the presence of iron (Fe) and also detected the presence of Cl, K, O, and C elements at approx. 2.5, 3.4, 0.5, and 0.3 keV in it, respectively. The presence of other elements was confirmed, which supported the idea that PEG stabilizes α-Fe_2O_3 NPs. However, the presence of K and Cl might be due to improper washing of α-Fe_2O_3 NPs. Using FE-SEM micrographs, the calculated particle size of α-Fe_2O_3 NPs shows good agreement with the particle size calculated from transmission electron microscopy (TEM) and powder X-ray diffraction analysis (vide infra).

A transmission electron microscopy (TEM) image of the synthesized α-Fe_2O_3 NPs at a resolution of 200 nm is shown in Figure 4. It is clearly seen from the TEM image that the morphology of the sample shows approximately spherical particles having a diameter ranging from 50 to 60 nm. Along

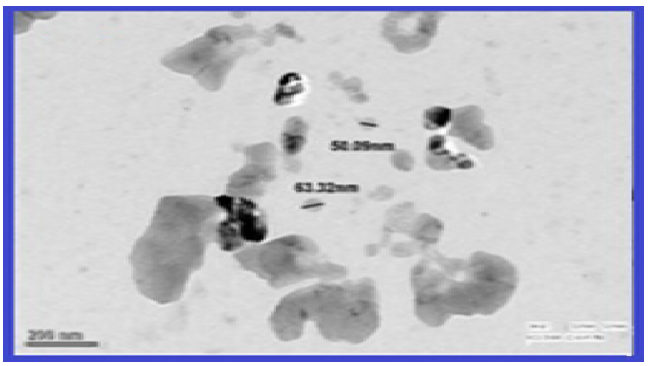

Figure 4. Transmission electron microscopy (TEM) image of α-Fe_2O_3 NPs.

with this, the two-dimensional (2-D) and three-dimensional (3-D) surface morphological analyses of synthesized α-Fe_2O_3 NPs by atomic force microscopy (AFM) in dynamic mode are also shown in Figure 5a,b. Figure 5a explains that the particles

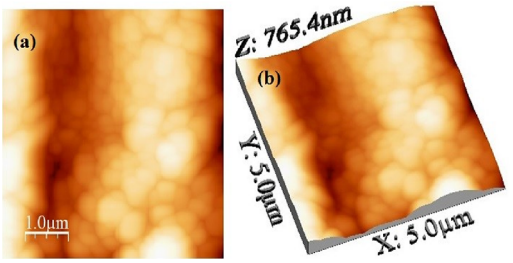

Figure 5. Atomic force microscopy (AFM) images: (a) 2-D and (b) 3-D surface morphological analysis of synthesized α-Fe_2O_3 NPs.

of α-Fe_2O_3 NPs are spherical having a diameter range of 60−80 nm and are well connected. Figure 5b represents the height profile of α-Fe_2O_3 NPs, which was found to be 765.40 nm. The root mean square (RMS) roughness of α-Fe_2O_3 NPs was found to be 28.64 nm.

3.3. Particle Size and Zeta Potential Estimation of Prepared α-Fe_2O_3 NPs. The hydrodynamic size and zeta potential (ZP) of α-Fe_2O_3 NPs were assessed by the DLS analysis. The hydrodynamic diameter involves the inorganic core, *i.e.*, metal and the functional group adsorbed onto the surface of NPs. Thus, the size estimated by DLS is larger due to the stabilization of α-Fe_2O_3 NPs by the functional groups of PEG. A plot for the size distribution of α-Fe_2O_3 NPs is shown in Figure 6a. It explains that the particles' size was distributed in the range of 70−100 nm, while most population falls at around 85 nm. Figure 6b shows that the zeta potential curve of α-Fe_2O_3 NPs was estimated between −100 and +100 mV. The zeta potential (ZP) investigation of the synthesized α-Fe_2O_3 NPs is an essential factor for deciding the surface charge on the NPs in the colloidal phase and their stability. The measured ZP value was -28 ± 18 mV, which demonstrates that the surface of α-Fe_2O_3 NPs is negatively charged and thus maintains their stability.[51] Hence, it can be assumed that a high ZP value leads to an increase in the physical stability of α-Fe_2O_3 NPs and further provides a versatile approach toward biomedical or pharmaceutical utility.

3.4. UV−Visible (UV−Vis) Spectroscopy Analysis of Prepared α-Fe_2O_3 NPs. The synthesized α-Fe_2O_3 NPs were also characterized using the UV−visible spectral analysis

https://doi.org/10.1021/acsomega.2c02083
ACS Omega 2022, 7, 21882−21890

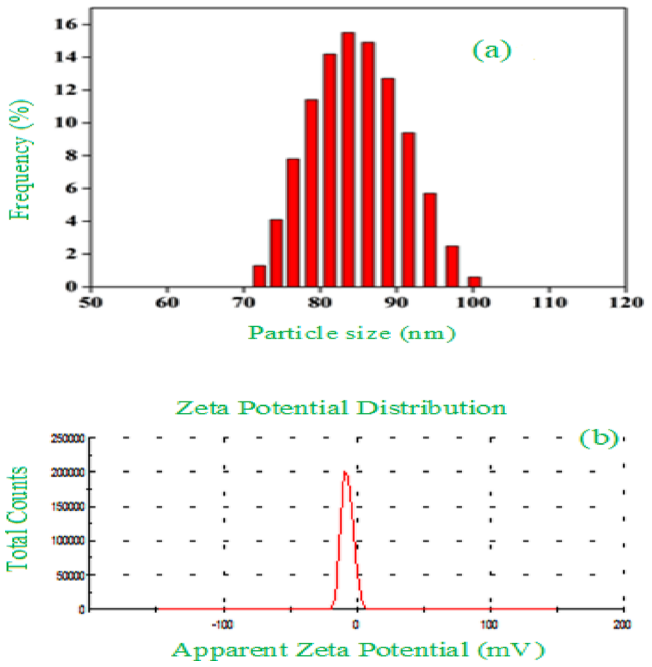

Figure 6. (a) Dynamic light scattering (DLS) analysis for particle size and distribution (b) zeta potential analysis of α-Fe_2O_3 NPs.

recorded in the wavelength range of 350−500 nm, as shown in Figure 7. The formation of α-Fe_2O_3 NPs using the $K_3[FeCl_6]$

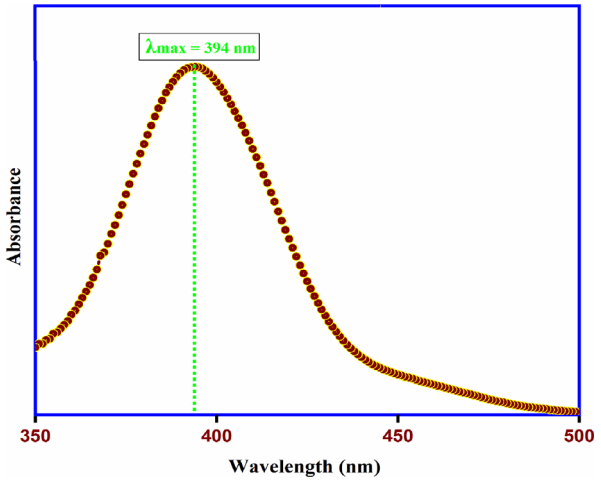

Figure 7. UV−visible absorption spectra of α-Fe_2O_3 NPs.

coordination complex was confirmed as the absorption peak was found at 394 nm. The present result correlates with the already reported results by many researchers.[52] The single and sharp peak at 394 nm in the UV−Vis absorption spectra also confirmed that the α-Fe_2O_3 NPs are of spherical morphology.[48,53]

3.5. FTIR Analysis of α-Fe_2O_3 NPs. The FTIR analysis was performed to gain information about the functional groups adsorbed on the surface of α-Fe_2O_3 NPs. The FTIR spectra of the synthesized α-Fe_2O_3 NPs were recorded, pellets were made using spectroscopic grade KBr in the wavenumber range of 4000 to 500 cm^{-1} in the diffuse reflectance mode, and the interaction of synthesized α-Fe_2O_3 NPs with functional groups of LAA and PEG was investigated. Figure 8 clearly exhibits several absorption bands at 3420, 2930, 1625, 1465, 1270, 973,

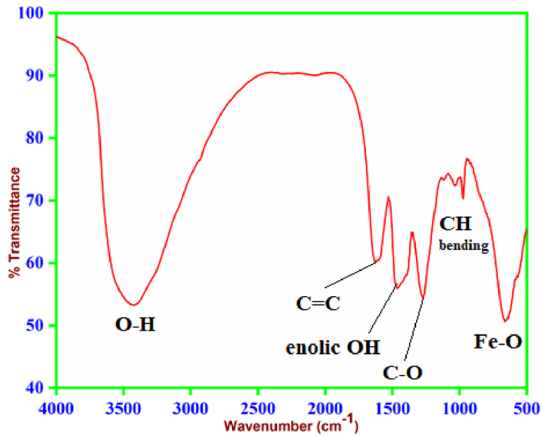

Figure 8. FTIR spectra of α-Fe_2O_3 NPs.

665, and 570 cm^{-1}. The broad absorption band at 3420 cm^{-1} corresponds to the −OH stretching frequency, which confirms the presence of hydrogen bonding between LAA and PEG-coated α-Fe_2O_3 NPs, while the band at 2930 cm^{-1} represents the sp^3 −CH stretching frequency of LAA.[54] Bands located at 1625 and 1465 cm^{-1} are due to the carbon−carbon double bond and the enolic hydroxy group of LAA, respectively. A band at 1270 cm^{-1} is due to the C−O stretching vibration of LAA.[55] A weak band at 973 cm^{-1} is due to the out-of-plane bending vibration of C−H of the adsorbed PEG on the surface of α-Fe_2O_3 NPs. The absorption bands in the fingerprint region at 665 and 573 cm^{-1} are due to the Fe−O interaction of α-Fe_2O_3 NPs.[48,56]

3.6. *In Vitro* Cell Line Assay for the Cytotoxicity of α-Fe_2O_3 NPs. The viability of cells with α-Fe_2O_3 NPs was investigated against human lung cancer cells (A549 cell line, ATCC, Rockville, Manassas, VA, USA) as a model system. The cells were seeded at a seed density of 7500 cells/well in 96-well plates. The cells were seeded in a CO_2 atmosphere incubated at 37 °C and a humidified atmosphere of 5% (v/v) CO_2 for a day until 80% confluency was reached. Dulbecco's modified Eagle medium (DMEM) supplemented with 2 mM L-glutamine and 10% (v/v) fetal bovine serum (FBS) was used as a culture medium.[23] Phosphate-buffered saline (PBS; 0.01 M) was used to rinse the cultured cells, and then the cells were treated with a solution of TRY-EDTA followed by DMEM for resuspension. Later on, the A549 cells were treated with α-Fe_2O_3 NPs at a concentration range of 15−60 μg/mL. The A549 cells were again incubated at 37 °C in 5% CO_2 for the next day, and a control group corresponding to untreated cells with ethanol and acetic acid was formulated. After the treatment, cells were determined using an MTT assay in which the complex medium was removed from the wells and the cells were washed with phosphate-buffered saline (PBS). The MTT assay reagent, made up in the medium to a final concentration of 0.5 mg/mL, was added to the wells of 96-well plates. The plates were incubated for half an hour to 3 h at 37 °C until an intracellular purple formazan crystal was visible under a microscope. MTT was removed and solubilizing solution (200 μL of DMSO) was added to cells. The absorbance of the solution was monitored by a UV−visible spectrophotometer with a microplate at a fixed wavelength using a microplate reader (BIO-RAD Model 680). For statistical investigation, GraphPad Prism was used. The cytotoxicity of α-Fe_2O_3 NPs was investigated against A549

https://doi.org/10.1021/acsomega.2c02083
ACS Omega 2022, 7, 21882−21890

lung cancer cell lines in the range of 15−60 μg/mL using a reference blank in terms of percentage cell viability. The percentage (%) cell viability was calculated by using the following formula:[40]

$$\%\text{cell viability} = \frac{[(\text{control absorbance}) - (\text{test absorbance})]}{(\text{control absorbance})} \times 100$$

The percentage (%) cell viability was estimated as a measure of the cytotoxicity of α-Fe_2O_3 NPs at different concentrations, *i.e.*, 15 to 60 μg/mL. The percentage (%) viability of A549 cells treated with α-Fe_2O_3 NPs was decreased at a significant level when compared to control blank. The standard graph of A549 lung cancer cell lines loaded with α-Fe_2O_3 NPs is plotted in Figure 9a. Moreover, the main difference between a conventional drug whose nature is similar to α-Fe_2O_3 NPs and the prepared α-Fe_2O_3 NPs is that it reduces the adverse effects or severity. However, depending upon doses, both of them show different percentages (%) of cell viability. The efficacy of both can be compared by calculating the 50% inhibitory concentration, *i.e.*, IC_{50} value, the concentration required for 50% inhibition *in vitro* of α-Fe_2O_3 NPs. The calculated IC_{50} value of ≤30.0 μg/mL indicated the best therapeutic efficacy in the biological system, *i.e.*, against human lung cancer cells (A549 cell lines). Figure 9b clearly shows that the % cell viability decreases with an increase in concentration (μg/mL), indicating that the synthesized α-Fe_2O_3 NPs were active against A549 cell lines. Therefore, we can say that α-Fe_2O_3 NPs may be beneficial from a drug design perspective with respect to the standard drug Adriamycin. Microscopic observation of cells treated with α-Fe_2O_3 NPs with increased concentration was carried out as an appropriate control, as shown in Figure 9c. The treatment of A549 lung cancer cell lines with α-Fe_2O_3 NPs inhibited the proliferation of cell lines in a time-dependent and dose-dependent manner. It was observed that the morphology was lost effectively with the treatment of α-Fe_2O_3 NPs at higher concentrations and debris was collected at a concentration range of 15 to 60 μg/mL with the most complete destruction of cells.[39,40]

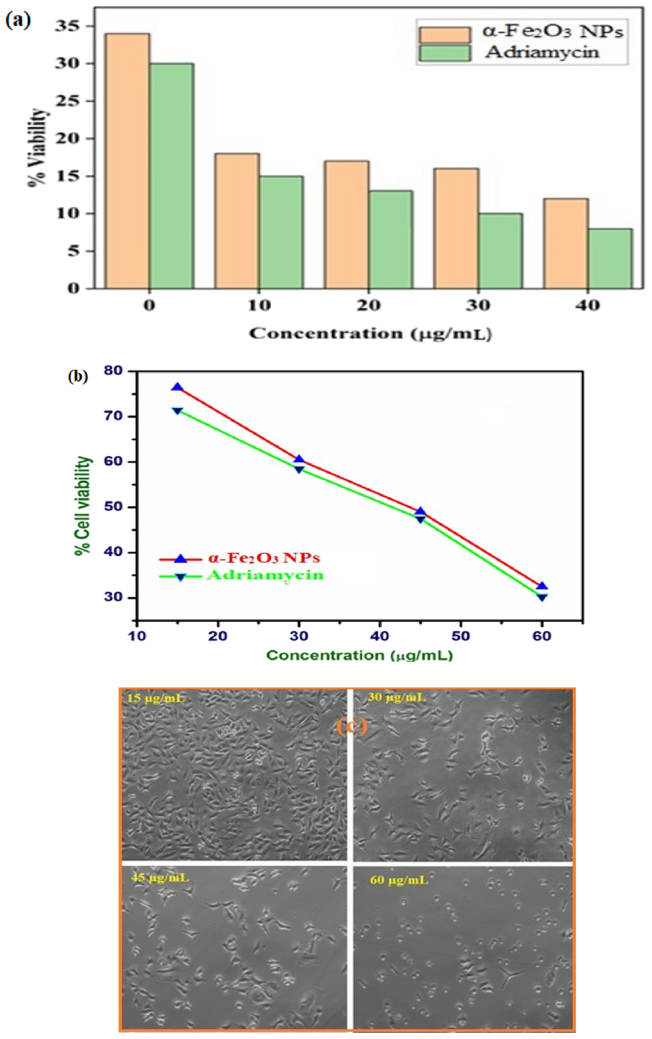

Figure 9. (a) Cell viability of α-Fe_2O_3 NPs, (b) effect of dose of α-Fe_2O_3 NPs and Adriamycin on human A549 lung cancer cells, and (c) microscopic images of α-Fe_2O_3 NPs against A549 lung cancer cell lines (copyright 2022 Abbas Ali Mehdi).

4. CONCLUSIONS

The present work deals with the synthesis of α-Fe_2O_3 NPs using LAA and PEG as reducing and stabilizing agents, respectively. The formation of α-Fe_2O_3 NPs was preliminarily confirmed by obtaining a reddish-brown colloidal solution. A sharp plasmonic band at 394 nm was observed in the absorption spectra, which further confirms the formation of α-Fe_2O_3 NPs. From the morphological analysis, it has been clear that α-Fe_2O_3 NPs are of spherical shape with the average size ranging from 40 to 60 nm. The presence of iron in α-Fe_2O_3 NPs was confirmed by EDX analysis. However, remaining peaks in the EDX profile show that α-Fe_2O_3 NPs are stabilized by several functional groups. Further, this aspect is also confirmed by FTIR and DLS analyses. Several bands in the FTIR spectra prove that α-Fe_2O_3 NPs are stabilized by LAA and PEG. The hydrodynamic size of α-Fe_2O_3 NPs was found to be 85 nm with a zeta potential of −28 ± 18 mV. It shows that α-Fe_2O_3 NPs are physically stable with negative surface charge density, and consequently, they provide a versatile approach toward biomedical or pharmaceutical utility. These α-Fe_2O_3 NPs were subjected to cytotoxicity against human lung cancer cells (A549 cell line). The calculated IC_{50} value of ≤30.0 μg/mL indicated the best therapeutic efficacy in the biological system. Conclusively, the prepared α-Fe_2O_3 NPs were successfully utilized in the treatment of human lung cancer cells (A549 cell line) after several proper clinical trials.

AUTHOR INFORMATION

Corresponding Author

Radhey Mohan Naik − *Department of Chemistry, University of Lucknow, Lucknow 226007 U.P., India*; orcid.org/0000-0003-1782-9125; Email: radheynaik@gmail.com.

Authors

Indresh Kumar − *Department of Chemistry, University of Lucknow, Lucknow 226007 U.P., India*

Rashmi Nayak − *Plant Diversity Systematics and Herbarium Division, CSIR-National Botanical Research Institute, Lucknow 226001 U.P., India*

Lal Babu Chaudhary − *Plant Diversity Systematics and Herbarium Division, CSIR-National Botanical Research Institute, Lucknow 226001 U.P., India*

https://doi.org/10.1021/acsomega.2c02083
ACS Omega 2022, 7, 21882−21890

Vashist Narayan Pandey − *Experimental Botany and Nutraceutical Laboratory, Department of Botany, DDU Gorakhpur University, Gorakhpur 273009 U.P., India*
Sheo K. Mishra − *Department of Physics, Indira Gandhi National Tribal University, Amarkantak 484887 M.P., India*
Narendra Kumar Singh − *Department of Chemistry, University of Lucknow, Lucknow 226007 U.P., India*
Abhishek Srivastava − *Department of Chemistry, GLA University, Mathura 281406 U.P., India*
Surendra Prasad − *School of Biological and Chemical Sciences, Faculty of Science, Technology and Environment, University of the South Pacific, Suva, Fiji*

Complete contact information is available at: https://pubs.acs.org/10.1021/acsomega.2c02083

Author Contributions

All the authors contributed equally to this work.

Notes

The authors declare no competing financial interest.

■ ACKNOWLEDGMENTS

The authors are highly thankful to the Head, Department of Chemistry, University of Lucknow, Lucknow, India, for providing infrastructure to perform the experiments including UV−visible double-beam spectrophotometry and FTIR analysis. The authors are thankful to Sophisticated Analytical Instrument Facility (SAIF), Babasaheb Bhimrao Ambedkar University, Lucknow, India, for providing dynamic light scattering facilities. The authors are also thankful to the Director and *Dr. Abbas Ali Mehdi*, Advanced Research Lab, King George Medical University, Lucknow, India, for evaluation and discussion about the cell culture system. The authors are also thankful to *Dr. Shubodh Kumar,* Birbal Sanhi Institute of Palaeosciences, Lucknow, for the FE-SEM analysis, *Prof. B. Das* and *Dr. R. R. Awasthi*, Department of Physics, University of Lucknow, India, for the AFM analysis, and SAIF, AIIMS, New Delhi, India, for the TEM analysis. *Prof. Surendr Prasad* is grateful to the University of the South Pacific for support in various ways. The authors are highly thankful to *Miss Chinky Gangwar* and *Miss Bushra Yaseen* for their valuable suggestions and editing.

■ REFERENCES

(1) Siegel, R. L.; Miller, K. D.; Jemal, A. Cancer statistics, 2019. *CA Cancer J. Clin.* **2019**, *69*, 7−34.
(2) Taratula, O.; Garbuzenko, O. B.; Chen, A. M.; Minko, T. Innovative strategy for treatment of lung cancer: targeted nanotechnology-based inhalation co-delivery of anticancer drugs and siRNA. *J. Drug Targeting* **2011**, *19*, 900−914.
(3) Ellis, D. I.; Cowcher, D. P.; Ashton, L.; O'Hagan, S.; Goodacre, R. Illuminating disease and enlightening biomedicine: Raman spectroscopy as a diagnostic tool. *Analyst* **2013**, *138*, 3871−3884.
(4) Shehzad, K.; Xu, Y.; Gao, C.; Duan, X. Three-dimensional macro-structures of two-dimensional nanomaterials. *Chem. Soc. Rev.* **2016**, *45*, 5541−5588.
(5) Pal, N.; Bhaumik, A. Soft templating strategies for the synthesis of mesoporous materials: inorganic, organic-inorganic hybrid and purely organic solids. *Adv. Colloid Interface Sci.* **2013**, *189-190*, 21−41.
(6) Bang, J. H.; Suslick, K. S. Applications of Ultrasound to the Synthesis of Nanostructured Materials. *Adv. Mater.* **2010**, *22*, 1039−1059.
(7) Mishra, S. K.; Tripathi, U.; Awasthi, R. R.; Shukla, R. K.; Kumar, I.; Mohan Naik, R.; Mishra, D. CTAB mediated synthesis of ZnO nanoparticles: Structural, optical and enhanced blue-green optical emission. *Mater. Today: Proc.* **2021**, 2229.
(8) Wang, Y.; Zhao, Q.; Han, N.; Bai, L.; Li, J.; Liu, J.; Che, E.; Hu, L.; Zhang, Q.; Jiang, T.; Wang, S. Mesoporous silica nanoparticles in drug delivery and biomedical applications. *Nanomed.: Nanotechnol., Biol., Med.* **2015**, *11*, 313−327.
(9) Chatterjee, D. K.; Diagaradjane, P.; Krishnan, S. Nanoparticle-mediated hyperthermia in cancer therapy. *Ther. Delivery* **2011**, *2*, 1001−1014.
(10) Xia, Y.; Yang, H.; Campbell, C. T., Nanoparticles for catalysis. In *Acc. Chem. Res.*, ACS Publications, 2013; Vol. *46*, pp. 1671−1672, DOI: 10.1021/ar400148q.
(11) Kang, H.; Wang, L.; O'Donoghue, M.; Cao, Y. C.; Tan, W., Nanoparticles for biosensors. In *Optical Biosensors*; Elsevier, 2008, pp. 583−621, DOI: 10.1016/B978-044453125-4.50017-6.
(12) Sharma, G.; Kodali, V.; Gaffrey, M.; Wang, W.; Minard, K. R.; Karin, N. J.; Teeguarden, J. G.; Thrall, B. D. Iron oxide nanoparticle agglomeration influences dose rates and modulates oxidative stress-mediated dose-response profiles in vitro. *Nanotoxicology* **2014**, *8*, 663−675.
(13) Renevier, N. M.; Lobiondo, N.; Fox, V. C.; Teer, D. G.; Hampshire, J. Performance of MoS_2/metal composite coatings used for dry machining and other industrial applications. *Surf. Coat. Technol.* **2000**, *123*, 84−91.
(14) Caruthers, S. D.; Wickline, S. A.; Lanza, G. M. Nanotechnological applications in medicine. *Curr. Opin. Biotechnol.* **2007**, *18*, 26−30.
(15) Xie, W.; Guo, Z.; Gao, F.; Gao, Q.; Wang, D.; Liaw, B. S.; Cai, Q.; Sun, X.; Wang, X.; Zhao, L. Shape-, size- and structure-controlled synthesis and biocompatibility of iron oxide nanoparticles for magnetic theranostics. *Theranostics* **2018**, *8*, 3284−3307.
(16) Saif, S.; Tahir, A.; Chen, Y. Green Synthesis of Iron Nanoparticles and Their Environmental Applications and Implications. *Nanomaterials* **2016**, *6*, 209.
(17) Sabir, F.; Zeeshan, M.; Laraib, U.; Barani, M.; Rahdar, A.; Cucchiarini, M.; Pandey, S. DNA Based and Stimuli-Responsive Smart Nanocarrier for Diagnosis and Treatment of Cancer: Applications and Challenges. *Cancers* **2021**, *13*, 3396.
(18) Barani, M.; Mukhtar, M.; Rahdar, A.; Sargazi, S.; Pandey, S.; Kang, M. Recent Advances in Nanotechnology-Based Diagnosis and Treatments of Human Osteosarcoma. *Biosensors* **2021**, *11*, 55.
(19) Barani, M.; Hosseinikhah, S. M.; Rahdar, A.; Farhoudi, L.; Arshad, R.; Cucchiarini, M.; Pandey, S. Nanotechnology in Bladder Cancer: Diagnosis and Treatment. *Cancers* **2021**, *13*, 2214.
(20) Arshad, R.; Barani, M.; Rahdar, A.; Sargazi, S.; Cucchiarini, M.; Pandey, S.; Kang, M. Multi-Functionalized Nanomaterials and Nanoparticles for Diagnosis and Treatment of Retinoblastoma. *Biosensors* **2021**, *11*, 97.
(21) Wu, W.; Jiang, C. Z.; Roy, V. A. L. Designed synthesis and surface engineering strategies of magnetic iron oxide nanoparticles for biomedical applications. *Nanoscale* **2016**, *8*, 19421−19474.
(22) Laurent, S.; Forge, D.; Port, M.; Roch, A.; Robic, C.; Vander Elst, L.; Muller, R. N. Magnetic Iron Oxide Nanoparticles: Synthesis, Stabilization, Vectorization, Physicochemical Characterizations, and Biological Applications. *Chem. Rev.* **2008**, *108*, 2064−2110.
(23) Gangwar, C.; Yaseen, B.; Nayak, R.; Praveen, S.; Singh, N. K.; Sarkar, J.; Banerjee, M.; Naik, R. M. Silver Nanoparticles Fabricated by Tannic Acid for their Antimicrobial and Anticancerous Activity. *Inorg. Chem. Commun.* **2022**, No. 109532.
(24) Ling, D.; Hyeon, T. Chemical design of biocompatible iron oxide nanoparticles for medical applications. *Small* **2013**, *9*, 1450−1466.
(25) Kumar, I.; Yaseen, B.; Gangwar, C.; Mishra, S. K.; Mohan Naik, R. Environmental benign synthesis and characterization of nickel oxide nanoparticles using chicken egg white as template and evaluations of their antibacterial/antifungal activities. *Mater. Today: Proc.* **2021**, *46*, 2272−2276.
(26) Kumar, I.; Yaseen, B.; Gangwar, C.; Yadav, R.; Mishra, S. K.; Mohan Naik, R. Ovalbumin mediated eco-friendly synthesis of silver

oxide nanoparticles and their antibacterial and antifungal studies. *Mater. Today: Proc.* **2021**, *46*, 2330−2334.
(27) Mishra, S. K.; Tripathi, U. K.; Awasthi, R. R.; Dubey, K. C.; Shukla, R. K.; Kumar, I.; Naik, R. M.; Mishra, D. P. Sol-gel derived Al-doped ZnO nanoplates: Structural and optical properties. *Mater. Today: Proc.* **2021**, *46*, 2197−2200.
(28) Peternele, W. S.; Monge Fuentes, V.; Fascineli, M. L.; Rodrigues da Silva, J.; Silva, R. C.; Lucci, C. M.; Bentes de Azevedo, R. Experimental Investigation of the Coprecipitation Method: An Approach to Obtain Magnetite and Maghemite Nanoparticles with Improved Properties. *J. Nanomater.* **2014**, *2014*, No. 682985.
(29) Ge, S.; Shi, X.; Sun, K.; Li, C.; Uher, C.; Baker, J. R.; Banaszak Holl, M. M.; Orr, B. G. Facile Hydrothermal Synthesis of Iron Oxide Nanoparticles with Tunable Magnetic Properties. *J. Phys. Chem. C* **2009**, *113*, 13593−13599.
(30) Ali Dheyab, M.; Aziz, A. A.; Jameel, M. S. Recent advances in inorganic nanomaterials synthesis using sonochemistry: a comprehensive review on iron oxide, gold and iron oxide coated gold nanoparticles. *Molecules* **2021**, *26*, 2453.
(31) Suslick, K. S.; Hammerton, D. A.; Cline, R. E. Sonochemical hot spot. *J. Am. Chem. Soc.* **1986**, *108*, 5641−5642.
(32) Kastrinaki, G.; Lorentzou, S.; Karagiannakis, G.; Rattenbury, M.; Woodhead, J.; Konstandopoulos, A. Parametric synthesis study of iron based nanoparticles via aerosol spray pyrolysis route. *J. Aerosol Sci.* **2018**, *115*, 96−107.
(33) Gangwar, C.; Yaseen, B.; Kumar, I.; Singh, N. K.; Naik, R. M. Growth Kinetic Study of Tannic Acid Mediated Monodispersed Silver Nanoparticles Synthesized by Chemical Reduction Method and Its Characterization. *ACS Omega* **2021**, *6*, 22344−22356.
(34) Yaseen, B.; Gangwar, C.; Kumar, I.; Sarkar, J.; Naik, R. M. Detailed Kinetic and Mechanistic Study for the Preparation of Silver Nanoparticles by a Chemical Reduction Method in the Presence of a Neuroleptic Agent (Gabapentin) at an Alkaline pH and its Characterization. *ACS Omega* **2022**, *7*, 5739−5750.
(35) Kumar, I.; Gangwar, C.; Yaseen, B.; Pandey, P. K.; Mishra, S. K.; Naik, R. M. Kinetic and Mechanistic Studies of the Formation of Silver Nanoparticles by Nicotinamide as a Reducing Agent. *ACS Omega* **2022**, *7*, 13778−13788.
(36) Chen, J.; He, S.; Liu, Y.; Qiao, Z.; Huang, B.; Li, X.; Hao, Q.; Huang, H.; Yang, G. Highly active catalysts based on 3D hierarchically ordered porous carbon with entrapped Fe2O3 nanoparticles for the thermal decomposition of ammonium perchlorate. *Appl. Surf. Sci.* **2021**, *538*, No. 148148.
(37) Thenmozhi, T.; Nadella, R.; Megala, R.; Nannepaga, J. S. Biosynthesis and Characterization of Iron Oxide Nanoparticles via Syzygium aromaticum Extract and Determination of Its Cytotoxicity against Human Breast Cancer Cell Lines. *J. Nanosci. Nanotechnol.* **2019**, *5*, 587−592.
(38) Calero, M.; Chiappi, M.; Lazaro-Carrillo, A.; Rodríguez, M. J.; Chichón, F. J.; Crosbie-Staunton, K.; Prina-Mello, A.; Volkov, Y.; Villanueva, A.; Carrascosa, J. L. Characterization of interaction of magnetic nanoparticles with breast cancer cells. *J. Nanobiotechnol.* **2015**, *13*, 16.
(39) Watanabe, M.; Yoneda, M.; Morohashi, A.; Hori, Y.; Okamoto, D.; Sato, A.; Kurioka, D.; Nittami, T.; Hirokawa, Y.; Shiraishi, T.; Kawai, K.; Kasai, H.; Totsuka, Y. Effects of Fe_3O_4 Magnetic Nanoparticles on A549 Cells. *Int. J. Mol. Sci.* **2013**, *14*, 15546−15560.
(40) AlSalhi, M. S.; Devanesan, S.; Shanmugam, P.; Kim, Y. O.; Kwon, J. T.; Kim, H. J. Synthesis and biocompatible role of hierarchical structured carbon nanoplates incorporated α-$Fe_{(2)}O_{(3)}$ nanocomposites for biomedical applications with respect to cancer treatment. *Saudi J. Biol. Sci.* **2020**, *27*, 588−593.
(41) Fahmi, M. Z.; Chang, J.-Y. A facile strategy to enable nanoparticles for simultaneous phase transfer, folate receptor targeting, and cisplatin delivery. *RSC Adv.* **2014**, *4*, 56713−56721.
(42) Ebrahimi, E.; Akbarzadeh, A.; Abbasi, E.; Khandaghi, A. A.; Abasalizadeh, F.; Davaran, S. RETRACTED ARTICLE: Novel drug delivery system based on doxorubicin-encapsulated magnetic nanoparticles modified with PLGA-PEG1000 copolymer. *Artif Cells Nanomed Biotechnol* **2016**, *44*, 290−297.
(43) An, Q.; Sun, C.; Li, D.; Xu, K.; Guo, J.; Wang, C. Peroxidase-like activity of Fe_3O_4@carbon nanoparticles enhances ascorbic acid-induced oxidative stress and selective damage to PC-3 prostate cancer cells. *ACS Appl. Mater. Interfaces* **2013**, *5*, 13248−13257.
(44) Byers, T.; Perry, G. Dietary carotenes, vitamin C, and vitamin E as protective antioxidants in human cancers. *Annu. Rev. Nutr.* **1992**, *12*, 139−159.
(45) Badu-Boateng, C.; Naftalin, R. J. Ascorbate and ferritin interactions: Consequences for iron release in vitro and in vivo and implications for inflammation. *Free Radical Biol. Med.* **2019**, *133*, 75−87.
(46) Fam, S. Y.; Chee, C. F.; Yong, C. Y.; Ho, K. L.; Mariatulqabtiah, A. R.; Tan, W. S. Stealth Coating of Nanoparticles in Drug-Delivery Systems. *Nanomaterials* **2020**, *10*, 787.
(47) Wang, Z.; Zhang, K.; Fei, T.; Gu, F.; Han, D. α-Fe_2O_3/NiO heterojunction nanorods with enhanced gas sensing performance for acetone. *Sens. Actuators, B* **2020**, *318*, No. 128191.
(48) Abbas, G.; Singh, K. B.; Kumar, N.; Shukla, A.; Kumar, D.; Pandey, G. Efficient anticarcinogenic activity of α-Fe_2O_3 nanoparticles: In-vitro and computational study on human renal carcinoma cells HEK-293. *Mater. Today Commun.* **2021**, *26*, No. 102175.
(49) Wang, B.; Chen, J. S.; Wu, H. B.; Wang, Z.; Lou, X. W. Quasiemulsion-Templated Formation of α-Fe_2O_3 Hollow Spheres with Enhanced Lithium Storage Properties. *J. Am. Chem. Soc.* **2011**, *133*, 17146−17148.
(50) Kuang, Y.; Wang, Q.; Chen, Z.; Megharaj, M.; Naidu, R. Heterogeneous Fenton-like oxidation of monochlorobenzene using green synthesis of iron nanoparticles. *J. Colloid Interface Sci.* **2013**, *410*, 67−73.
(51) Banerji, B.; Pramanik, S. K.; Mandal, S.; Maiti, N. C.; Chaudhuri, K. Synthesis, characterization and cytotoxicity study of magnetic (Fe_3O_4) nanoparticles and their drug conjugate. *RSC Adv.* **2012**, *2*, 2493−2497.
(52) Dadashi, S.; Poursalehi, R.; Delavari, H. Structural and Optical Properties of Pure Iron and Iron Oxide Nanoparticles Prepared via Pulsed Nd:YAG Laser Ablation in Liquid. *Procedia Mater. Sci.* **2015**, *11*, 722−726.
(53) Murgueitio, E.; Cumbal, L.; Abril, M.; Izquierdo, A.; Debut, A.; Tinoco, O. Green Synthesis of Iron Nanoparticles: Application on the Removal of Petroleum Oil from Contaminated Water and Soils. *J. Nanotechnol.* **2018**, *2018*, 4184769.
(54) Sreeja, V.; Jayaprabha, K. N.; Joy, P. A. Water-dispersible ascorbic-acid-coated magnetite nanoparticles for contrast enhancement in MRI. *Appl. Nanosci.* **2015**, *5*, 435−441.
(55) Zeng-guo, F.; Sanping, Z. Synthesis and characterization of biodegradable hydrogels based on photopolymerizable acrylate-terminated CL-PEG-CL macromers with supramolecular assemblies of α-cyclodextrins. *Polymer* **2003**, *44*, 5177−5186.
(56) Iraj, K.; Mosivand, S. Phase Transition of Electrooxidized Fe_3O_4 to gamma and alpha-Fe_2O_3 Nanoparticles Using Sintering Treatment. *Acta Phys. Pol. A* **2014**, *125*, 1210−1214.

https://doi.org/10.1021/acsomega.2c02083
ACS Omega 2022, 7, 21882−21890